

## Article

# Influence of Radial Flows on Power Density and Gas Stream Pressure Drop of Tubular Solid Oxide Fuel Cells

Abdellah Essaghouri <sup>†</sup>, Zezhi Zeng <sup>†</sup>, Bingguo Zhao, Changkun Hao, Yuping Qian, Weilin Zhuge and Yangjun Zhang <sup>\*</sup>

State Key Laboratory of Automotive Safety and Energy, School of Vehicle and Mobility, Tsinghua University, Beijing 100084, China

<sup>\*</sup> Correspondence: yjzhang@tsinghua.edu.cn

<sup>†</sup> These authors contributed equally to this work.

**Abstract:** The development of solid oxide fuel cells (SOFCs) for powering vehicles requires high power densities. The radial flows generated by the insert structures in SOFC fuel channels could improve the power density by facilitating the fuel to enter the porous anode for electrochemical reactions. In this paper, we developed a 2D axisymmetric numerical model to examine the influence of a convergent conical ring insert on the flow and mass transfer characteristics in a tubular SOFC. The mass transfer conductance of fuel was analyzed and proposed to quantify the performance of different insert designs. The effects of the radius and offset angle of the convergent conical ring insert were examined and analyzed. We demonstrate that increasing the insert radius could increase the fuel mass transfer conductance and effectively improve the net output power of the tubular SOFC by 12% while the offset angle of the inserts exhibits a negligible impact on the fuel mass transfer conductance. Increasing the offset angle could help reduce the gas-phase pressure drop in fuel channels by 42%. The present study helps improve our understanding of the relationship between fuel mass transfer conductance and electrochemical reactions. It also proposes channel design methods based on mass transfer conductance for high-power-density solid oxide fuel cells.

**Keywords:** solid oxide fuel cell; radial flow; mass transfer; electrochemical reactions; power density



**Citation:** Essaghouri, A.; Zeng, Z.; Zhao, B.; Hao, C.; Qian, Y.; Zhuge, W.; Zhang, Y. Influence of Radial Flows on Power Density and Gas Stream Pressure Drop of Tubular Solid Oxide Fuel Cells. *Energies* **2022**, *15*, 7875. <https://doi.org/10.3390/en15217875>

Academic Editor: Attilio Converti

Received: 29 September 2022

Accepted: 20 October 2022

Published: 24 October 2022

**Publisher's Note:** MDPI stays neutral with regard to jurisdictional claims in published maps and institutional affiliations.



**Copyright:** © 2022 by the authors. Licensee MDPI, Basel, Switzerland. This article is an open access article distributed under the terms and conditions of the Creative Commons Attribution (CC BY) license (<https://creativecommons.org/licenses/by/4.0/>).

## 1. Introduction

Solid oxide fuel cells are among the most promising technologies that generate clean energy for a vast range of industrial applications, including automotive and aircraft industries [1–3]. The operating temperature of SOFCs varies depending on the electrolyte material and can reach up to 1000 °C [4]. Because of their high operating temperature, SOFCs can operate on a variety of fuels, such as hydrogen, methane, and diesel [5–7]. Furthermore, SOFCs are capable of reforming hydrocarbon fuels through the methane steam reforming reaction, water–gas reaction, and dry reforming, making them a strong candidate for future auxiliary power units [8–10]. SOFCs came in a variety of structures, the most common of which are the planar and tubular designs, which have been extensively investigated. These geometrical designs have different advantages. The tubular SOFC, for instance, has been recommended to power vehicles due to its compact design, short start-up time, and high performance comparable to other types.

However, to meet the demands of the automotive and aviation industries, SOFCs still require further improvements in terms of power density [11]. Improving the SOFC stacks' power density will increase the potential application of this technology in the automotive industry. While the long start-up time has been significantly reduced [12–14], the thermal cycling durability has been greatly enhanced in recent research [15–17]. In particular, the low stack power density is primarily due to improper gas flow management and geometrical design. Increasing the net power density of SOFCs will boost their application

by reducing their size and cost [18]. The flow field and mass transfer characteristics are critical to the SOFC stack performance. An appropriate flow field design is required to increase the local concentration of reactants inside the porous electrodes and enhance the electrochemical reactions at the cell level. Previous research has intensively investigated the effect of the flow field on the electrochemical performance in SOFCs.

Several factors affect the flow field inside the SOFC flow channels and porous electrodes. The inlet design is one of these factors. Well-designed guided vanes, for instance, can distribute the gas flow more uniformly, improving the local gas concentration distribution, reducing the temperature gradient, and resulting in an 11% increase in the peak power density, as reported [19]. Another study compared two inlet designs, one with a parallel distribution design and the other with a narrow distribution design. They found that the narrow distribution design improves the gas distribution and enhances the reforming reaction rates. At the same time, the power density was increased by about 6% [20]. Another related study compared different inlet designs in a serpentine flow channel. They reported that a triple-entry flow channel design could improve the SOFC performance by more than 5% compared to single- and double-entry serpentine designs [21]. Yu et al. [22] conducted a comprehensive analysis of the effect of an inlet/outlet manifold design on the airflow distribution of a micro-tubular SOFC stack using various flow manifold structures, such as the single and double inlet/outlet Z-type. Their analysis revealed that the double inlet/outlet Z-type helped enhance the distribution quality of the airflow more than the single inlet/outlet line-type and Z-type. A 49 tubular SOFC unit stack was the subject of a later study that compared a line type with a single inlet/outlet, a U-type with a double inlet/outlet, and a modified type with an external airflow path [23]. They found that with the external airflow channel design, the SOFC stack performance was improved by delivering additional air and enhancing the distribution quality of gas compared to the other types.

The flow channel design is another factor affecting species diffusion to the gas diffusion layer and directly influences the SOFC electrochemical performance. In this aspect, various approaches have been proposed. The flow channel design has been widely investigated for its potential to affect the flow field and mass transfer characteristics. Various shape designs of flow channels, such as triangular, trapezoidal, and rectangular, have been proposed. According to [24], the triangular and rectangular channel designs produced 22% and 27% more power density than the trapezoidal channel design, respectively. A recent study examined the influence of channel height on a MOLB-type SOFC power density per unit area and unit volume [25]. This study reported a slight increase from 0.385 to 0.395 ( $W/cm^2$ ) in the power density per unit area as the channel's height increased from 1 to 2 mm due to the wide electrochemical zone. In contrast, the power density per unit volume dropped from 1.38 to 1.05 ( $W/cm^3$ ) since the channel's height is proportional to the length of the current path. In a later study, two different interconnector designs—a straight channel interconnector (SCI) and a beam and slot interconnector (BSI)—were used to compare the electrical performance of an anode-supported SOFC stack [26]. They reported that, under the exact same operating conditions, the peak power density of the BSI stack design was higher than that of the SCI stack design at 650 and 800 °C, respectively, by 13.2% and 28.5%. A similar study compared the power densities of a parallel straight channel to a serpentine channel SOFC stack [27]. This study revealed that the serpentine design of the channel improved the power density and fuel efficiency at the cost of a high gas-phase pressure drop.

Insert structures are another way to change the flow field in SOFCs. The primary use of these inserts is to induce and or intensify secondary flows. In the literature, secondary flow is usually defined as the cross-sectional flow normal to the main flow [28]. This method has the capability to enhance the convective mass transfer and reactant mixing, which increases the electrochemical reaction rates by facilitating the fuel diffusion to reach the active electrode layer easily. One study suggested that replacing the straight cathode rib channel with a porous current collector could result in a 6.3% higher power density and an

8.6% increase in the electrical efficiency over the conventional design [29]. A recent study found that the use of a Ni-mesh wire inside the anode fuel channel increased the peak power density by 14% [19]. Canavar et al. conducted an experimental study in which they placed a woven Ni-mesh insert in the fuel channel of a tubular SOFC. They reported a 36% enhancement in the peak output power density compared to the conventional design [30]. These studies, as expected, demonstrated that the secondary flow generated by these structures could significantly improve the electrochemical reactions in SOFCs. Our early research examined the influence of recirculating flows in the air channels on heat transfer characteristics [31]. However, there have been few discussions on how the secondary flow affects the mass transfer characteristics. Our recent study compared the influence of radial and circumferential flows on the power density and gas-phase pressure drop of tubular SOFCs [32]. We showed that only the radial flow can efficiently enhance the power density while the circumferential flow has a trivial effect on the electrochemical reactions. We also conducted an initial qualitative analysis of the mass transfer characteristics of radial flows [33]. However, a parameter is still needed to quantitatively describe the mass transfer enhancement of radial flows in the fuel channel and porous anode and its influence on the power density. The design strategies for the inserts inside the fuel channel of the tubular SOFC also need further investigation.

This study examined the effect of radial secondary flows on the mass transfer characteristics in tubular SOFCs. In detail, we analyzed the influence of radial flows induced by a convergent conical ring insert on the fuel concentration and vorticity distributions, and their impacts on the electrochemical reactions. The impact of the radius and offset angle of the conical ring inserts on the net power density improvements and pump power demands of the tubular SOFC are then discussed and analyzed. We proposed mass transfer conductance of fuel to quantify the performance by evaluating the ability of the insert geometric variables to improve the electrochemical performance. Finally, a design strategy is proposed for higher output power and lower pump power demands for the tubular SOFC.

## 2. Model Description

### 2.1. Geometry Description

The model used in this study is a two-dimensional and axisymmetric multiphysics model based on an anode-supported tubular solid oxide fuel cell geometry. Table 1 lists the geometrical details and Figure 1 depicts the geometrical setup. This research presents a parametric study to investigate the effect of various geometrical variables of the insert structure inside the anode channel of the tubular SOFC on the flow field and mass transfer characteristics. The insert structure is a convergent conical ring with an offset angle,  $\alpha$ , which varies from  $0^\circ$  to  $21^\circ$  degrees. The radius of the conical ring insert is expressed as  $R_{cr}$  while the gap is defined as the space between the conical rings and the interface between the anode and fuel channel, as illustrated in Figure 1.

**Table 1.** The geometric parameters of the tubular solid oxide fuel cells investigated in this study.

Parameters	Symbols	Values	Units
Anode inner radius	$R_0$	3.5	mm
Cathode outer radius	$R_c$	10	mm
Cylindrical rod radius	$R_i$	1	mm
Anode thickness	$t_a$	2	mm
Electrolyte thickness	$t_e$	50	$\mu\text{m}$
Cathode thickness	$t_c$	250	$\mu\text{m}$
Reaction layer thickness	$h_{rl}$	20	$\mu\text{m}$
Pitch	$P_{cr}$	5	mm
Total length	$L_t$	100	mm

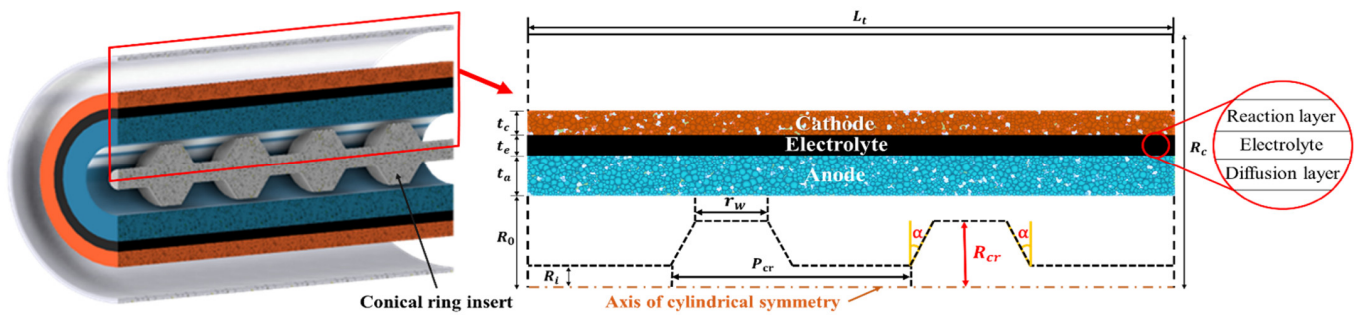


**Figure 1.** Schematic of a tubular solid oxide fuel cell with a convergent conical ring insert.

## 2.2. Numerical Model

### 2.2.1. Chemical Reactions

We used hydrogen and carbon monoxide as fuel for the tubular SOFCs because they are the only reactants that directly participate in the electrochemical reaction at the triple-phase boundaries. Hydrogen and carbon monoxide are produced for the electrochemical reactions as the hydrocarbon fuel is reformed. The model considers the water–gas shift reaction, which generates additional hydrogen for electrochemical reactions within the anode. We only assume the electrochemical reduction of oxygen at the cathode side. This research aimed to investigate the effect of radial flow on the mass transfer characteristics of these reactants in the anode and fuel channel of a micro-tubular SOFC. The individual reaction and input parameters used in this study are listed in Tables 2 and 3.

**Table 2.** A summary of the reactions in the tubular SOFC.

Electrochemical Reactions in SOFC	
Hydrogen electrochemical oxidation	$\text{H}_2 + \text{O}^{2-} \rightarrow \text{H}_2\text{O} + 2\text{e}^-$
Oxygen electrochemical reduction	$\text{O}_2 + 4\text{e}^- \rightarrow 2\text{O}^{2-}$
Water–gas shift reaction	$\text{H}_2\text{O} + \text{CO} \leftrightarrow \text{H}_2 + \text{CO}_2$
Carbon monoxide electrochemical oxidation	$\text{CO} + \text{O}^{2-} \rightarrow \text{CO}_2 + 2\text{e}^-$

### 2.2.2. Electrochemical Reactions

The operational potential of a single cell,  $E_0$ , is determined as follows [34]:

$$E_0 = E^{\text{Nernst}} - \eta_{\text{act,a}} - \eta_{\text{act,c}} - \eta_{\text{ohm}} \quad (1)$$

where  $E^{\text{Nernst}}$  is the Nernst equilibrium potential, and  $\eta_{\text{act}}$  and  $\eta_{\text{ohm}}$  are the activation overpotentials and the ohmic loss while the subscripts a and c represent the anode and cathode, respectively. The activation overpotential at the anode and cathode is defined as:

$$\eta_{\text{act,a}} = \phi_s - \phi_l - E_{\text{eq,a}} \quad (2)$$

$$\eta_{\text{act,c}} = \phi_s - \phi_l - E_{\text{eq,c}} \quad (3)$$

where  $\phi$  represents the potential, whereas the subscript s and l represent the electron conducting electrodes (Ni/LSM) and electrolyte material (YSZ). The Nernst equilibrium potentials of reactants are defined as:

$$E_{\text{H}_2}^{\text{Nernst}} = 1.253 - 2.4516 \times 10^{-4}T + \frac{RT}{2F} \ln \left[ \frac{P_{\text{H}_2}}{P_{\text{H}_2\text{O}}} \sqrt{\frac{P_{\text{O}_2}}{P_{\text{atm}}}} \right] \quad (4)$$

$$E_{\text{CO}}^{\text{Nernst}} = 1.46713 - 2.4527 \times 10^{-4}T + \frac{RT}{2F} \ln \left[ \frac{P_{\text{CO}}}{P_{\text{CO}_2}} \sqrt{\frac{P_{\text{O}_2}}{P_{\text{atm}}}} \right] \quad (5)$$

where  $P$  represents the local gas partial pressure at the triple-phase boundaries (TPBs); the subscripts  $\text{H}_2$ ,  $\text{CO}$ ,  $\text{O}_2$ , and  $\text{CO}_2$  represent the specific gas components. The local

temperature is  $T$ ,  $R$  is the universal gas constant, and  $F$  is the Faraday constant. The open circuit voltage of SOFC is assumed to vary linearly with the temperature [35]. We calculated the activation overpotentials,  $\eta_{act}$ , using the concentration-dependent Butler–Volmer equations as follows [36]:

$$i_{a,H_2} = A_{v,a} i_{0,H_2} \left( \frac{P_{H_2}}{P_{H_2,ref}} \exp\left(\frac{\alpha_a n_a F \eta_{act,a}}{RT}\right) - \frac{P_{H_2O}}{P_{H_2O,ref}} \exp\left(-\frac{(1-\alpha_a) n_a F \eta_{act,a}}{RT}\right) \right) \quad (6)$$

$$i_{a,CO} = A_{v,a} i_{0,CO} \left( \frac{P_{CO}}{P_{CO,ref}} \exp\left(\frac{\alpha_a n_a F \eta_{act,a}}{RT}\right) - \frac{P_{CO_2}}{P_{CO_2,ref}} \exp\left(-\frac{(1-\alpha_a) n_a F \eta_{act,a}}{RT}\right) \right) \quad (7)$$

$$i_c = A_{v,c} i_{0,O_2} \left( \exp\left(\frac{\alpha_c n_c F \eta_{act,c}}{RT}\right) - \frac{P_{O_2}}{P_{O_2,ref}} \exp\left(\frac{(\alpha_c - 1) n_c F \eta_{act,c}}{RT}\right) \right) \quad (8)$$

$$i_{total} = i_{a,H_2} + i_{a,CO} \quad (9)$$

In this equation,  $i_0$  is the exchange current density ( $A/m^2$ ),  $F$  is the Faraday constant,  $n$  is the number of electrons transferred per mole in the electrochemical reaction,  $i_{total}$  is the anode total current density, and  $\alpha$  is the electronic transfer coefficient. The ohmic losses caused by electron/ion conduction are derived from the following equations:

$$i_l = -\sigma_{l,eff} \nabla \phi_l \quad (10)$$

$$i_s = -\sigma_{s,eff} \nabla \phi_s \quad (11)$$

where the effective conductivity is  $\sigma_{eff}$ . The following equations are the definitions of the effective conductivities of the electrolyte and porous electrodes:

$$\sigma_{l,eff} = \sigma_l \cdot \frac{V_l}{\tau_l} \quad (12)$$

$$\sigma_{s,eff} = \sigma_s \cdot \frac{V_s}{\tau_s} \quad (13)$$

where  $V$  represents the volume fraction and  $\tau$  represents the tortuosity. The water–gas shift reaction (WGS) rate is expressed as:

$$R^{WGS} = K_{sf} \left( P_{CO} P_{H_2O} - \frac{P_{H_2} P_{CO_2}}{K_{ps}} \right) \quad (14)$$

$$K_{sf} = 1.71 \times 10^{-2} \exp\left(-\frac{103191}{RT}\right) \quad (15)$$

$$K_{ps} = \exp(-0.2935Z^3 + 0.6351Z^2 + 4.1788Z + 0.3169) \quad (16)$$

$$Z = \frac{1000(K)}{T} - 1 \quad (17)$$

In this equation,  $K_{sf}$  denotes the pre-exponential coefficient of the water–gas shift (WGS) reaction and  $K_{ps}$  denote the equilibrium constant.

### 2.2.3. Momentum Transport

The velocity and pressure distributions of the gas mixture in the anode fuel channel are obtained by solving the steady-state continuity and Navier–Stokes equations as follows:

$$\nabla \cdot (\rho \mathbf{u}) = 0 \quad (18)$$

$$\rho(\mathbf{u} \cdot \nabla) \mathbf{u} = \nabla \cdot \left[ -P + \mu \left\{ \nabla \mathbf{u} + (\nabla \mathbf{u})^T - \frac{2}{3} (\nabla \cdot \mathbf{u}) \right\} \right] \quad (19)$$

where  $\rho$ ,  $\mu$ , and  $\mathbf{u}$  represent the gas mixture's dynamic viscosity, density, and velocity.  $P$  stands for pressure. Using the ideal gas law, we can obtain the density of a gas mixture:

$$\rho = \frac{PM}{RT} \quad (20)$$

where  $R$  represents the universal gas constant,  $M$  represents the molar mass, and  $T$  represents the temperature. Wilke's method [37] expresses the viscosity of the mixture within the porous electrode as:

$$\mu_{\text{mix}} = \sum_{i=1}^n \frac{x_i \mu_i}{\sum_{j=1}^n x_j \phi_{ij}} \quad (21)$$

The subscripts  $i$  and  $j$  denote different gas components, and  $\phi_{ij}$  is described as follows:

$$\phi_{ij} = \sqrt{\frac{M_i}{M_j}} \quad (22)$$

Equations (23) and (24) use the Brinkman equations to compute and obtain the velocity and pressure distributions inside the porous electrodes:

$$\nabla \cdot (\rho \mathbf{u}) = Q_m \quad (23)$$

$$\frac{\rho}{\varepsilon} (\mathbf{u} \cdot \nabla) \frac{\mathbf{u}}{\varepsilon} = \nabla \left[ -p + \frac{\mu}{\varepsilon} \left\{ \nabla \mathbf{u} + (\nabla \mathbf{u})^T - \frac{2}{3} (\nabla \cdot \mathbf{u}) \right\} \right] - \left( \frac{\mu}{k} + \frac{Q_m}{\varepsilon^2} \right) \cdot \mathbf{u} \quad (24)$$

where  $\varepsilon$  and  $k$  are the porosity and the permeability of the porous electrodes, respectively. As shown in Equation (24), the source term  $Q_m$  appears in the mass and momentum equations resulting from the electrochemical reactions.

#### 2.2.4. Mass Transport

Diffusion and convection are the primary causes of gas mixture mass transfer in SOFC. The species conservation equation describes and analyzes the concentration of each gas element of the multi-component mixture:

$$\nabla \cdot \left( -\rho \omega_i \sum D_{\text{eff},ij} \nabla x_j + (x_j - \omega_j) \frac{\nabla p}{\rho} \cdot \mathbf{u} \right) + \rho (\mathbf{u} \cdot \nabla) \omega_i = S_i \quad (25)$$

where  $\omega$  and  $S_i$  are the mass fraction and the source term resulting from the electrochemical and reforming reactions.  $M$  is the molar mass and  $v$  is the diffusion volume. We can calculate the molecular diffusion coefficients from:

$$D_{ij} = \frac{101 \cdot T^{1.75} \cdot \left( \frac{1}{M_i} + \frac{1}{M_j} \right)^{0.5}}{p \cdot (v_i^{1/3} + v_j^{1/3})^2} \quad (26)$$

The porosity ( $\varepsilon$ ) and tortuosity ( $\tau$ ) are used to rectify the effective diffusion coefficient as it is influenced by the porous material structure and reduced diffusivity in the porous electrodes:

$$D_{\text{eff},ij} = \frac{\varepsilon}{\tau} \left( \frac{D_{ij} D_{k,ij}}{D_{ij} + D_{k,ij}} \right) \quad (27)$$

The Knudsen diffusion coefficient is defined as:

$$D_{k,ij} = \frac{2}{3} r_p \sqrt{\frac{8RT}{\pi M_{ij}}} \quad (28)$$

where  $r_p$  is the average pore radius of the electrode.

#### 2.3. Boundary Conditions

Figure 2 depicts the boundary conditions used in micro-tubular solid oxide fuel cells. We used a uniform air mass flow rate at the cathode's air channel inlet, a uniform  $\text{H}_2$  and  $\text{CO}$  mass flow rate at the anode's fuel channel inlet, and the operating pressure at the fuel channel outlet. For all cases investigated, the  $\text{O}_2$ ,  $\text{H}_2$ , and  $\text{CO}$  mole fractions are specified as  $x_{\text{O}_2}$ ,  $x_{\text{H}_2}$ , and  $x_{\text{CO}}$ , respectively. The cathode surface is linked to the operating potential while the anode surface is linked to the zero potential. The insert walls are associated with a no-slip boundary condition. We assume that the temperature is constant

(800 °C) throughout SOFC. This simulation does not consider the carbon deposition in the porous anode.

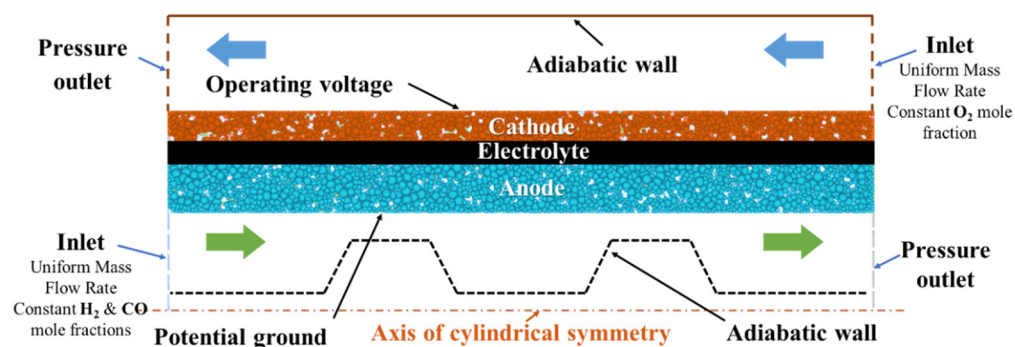


**Figure 2.** A summary of the simulation domain and boundary conditions of the tubular solid oxide fuel cells.

In order to increase the efficiency and accuracy of our numerical simulation, a fully structured mesh was constructed for the entire computational domain. In this study, we used about 425,000 mesh elements. We performed a mesh independence study to ensure that the steady-state solutions, such as the current density, reactant concentrations, and gas-phase pressure drop, are not affected by more than 1% after further mesh refinements.

**Table 3.** A summary of the parameters used in this study.

Parameters	Symbols	Values	Units	Ref.
Activation energy for the anode reaction	$E_a$	120	$\text{kJ}\cdot\text{mol}^{-1}$	[38]
Activation energy for the cathode reaction	$E_c$	130	$\text{kJ}\cdot\text{mol}^{-1}$	[38]
Electrode porosity	$\varepsilon$	0.35	-	[39]
Specific surface area, anode	$S_a$	$2.33 \times 10^5$	$\text{m}^{-1}$	[40]
Specific surface area, cathode	$S_c$	$2.46 \times 10^5$	$\text{m}^{-1}$	[40]
Permeability	$k$	$1 \times 10^{-10}$	$\text{m}^2$	[41]
Electrode tortuosity	$\tau$	4	-	[42]
Electrical conductivity, anode	$\sigma_{\text{Ni}}$	30,316	$\text{S}\cdot\text{m}^{-1}$	[43]
Electrical conductivity, cathode	$\sigma_{\text{LSM}}$	12,793	$\text{S}\cdot\text{m}^{-1}$	[43]
Ionic conductivity, electrolyte	$\sigma_{\text{YSZ}}$	2.2669	$\text{S}\cdot\text{m}^{-1}$	[43]
Diffusion volume, $\text{H}_2$	$v_{\text{H}_2}$	6.12	$\text{cm}^3$	[44]
Diffusion volume, CO	$v_{\text{CO}}$	18.0	$\text{cm}^3$	[44]
Diffusion volume, $\text{O}_2$	$v_{\text{O}_2}$	16.3	$\text{cm}^3$	[44]
Diffusion volume, $\text{CO}_2$	$v_{\text{CO}_2}$	26.7	$\text{cm}^3$	[44]
Diffusion volume, $\text{N}_2$	$v_{\text{N}_2}$	18.5	$\text{cm}^3$	[44]
Viscosity, CO	$\mu_{\text{CO}}$	$4.1877 \times 10^{-5}$	$\text{Pa}\cdot\text{s}$	[45]
Viscosity, $\text{O}_2$	$\mu_{\text{O}_2}$	$5.1343 \times 10^{-5}$	$\text{Pa}\cdot\text{s}$	[45]
Viscosity, $\text{CO}_2$	$\mu_{\text{CO}_2}$	$4.1904 \times 10^{-5}$	$\text{Pa}\cdot\text{s}$	[45]
Viscosity, $\text{N}_2$	$\mu_{\text{N}_2}$	$4.3529 \times 10^{-5}$	$\text{Pa}\cdot\text{s}$	[45]
Effective pore radius	$r_p$	0.5	$\mu\text{m}$	[46]
Operating pressure	$P_{\text{atm}}$	101.325	kPa	[47]
Inlet Mass flow rate at the anode	$Q_{\text{fuel}}$	$4.42 \times 10^{-6}$	$\text{kg}\cdot\text{s}^{-1}$	-
Inlet velocity at the cathode	$U_{\text{air}}$	1.5	$\text{m}\cdot\text{s}^{-1}$	-
Inlet mole fraction, $\text{H}_2$	$x_{\text{H}_2}$	0.68	-	-
Inlet mole fraction, CO	$x_{\text{CO}}$	0.17	-	-
Inlet mole fraction, $\text{CO}_2$	$x_{\text{CO}_2}$	0.05	-	-
Inlet mole fraction, $\text{O}_2$	$x_{\text{O}_2}$	0.21	-	-
Inlet mole fraction, $\text{H}_2\text{O}$	$x_{\text{H}_2\text{O}}$	0.1	-	-
Reference temperature	$T_{\text{ref}}$	800	$^\circ\text{C}$	-
Operating potential	$E_0$	0.5	V	-

#### 2.4. Model Validation

The simulated results from our numerical model were developed using COMSOL Multiphysics and validated using the experimental data from Mirahmadi's study [39]. Figure 3 compares the polarization curve from our simulation and their experimental data. The operating conditions of direct internal reforming (DIR), gradual internal reforming (GIR), and pure hydrogen were examined and validated. The predicted current densities from our simulation at the given operating voltages are within 2% of the experimental data.

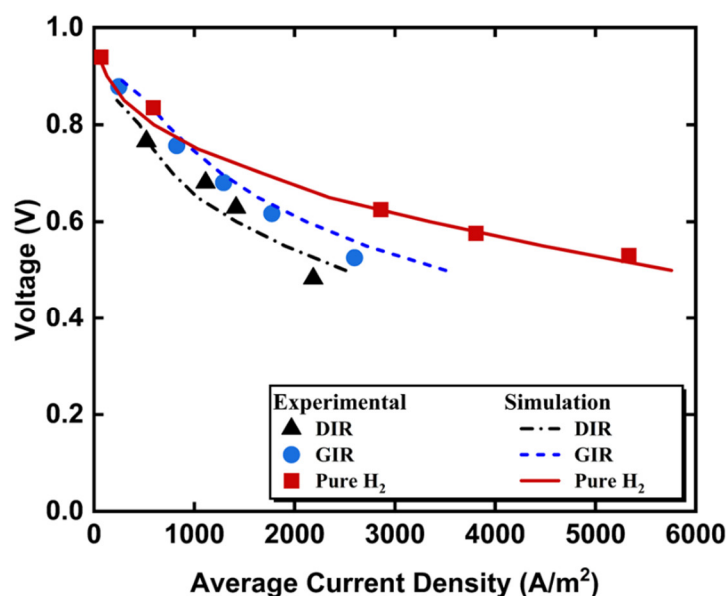


**Figure 3.** The operating voltage for tubular SOFC as a function of the current density at different operating conditions from our simulation and the experimental data [39].

### 3. Results and Discussion

The solid oxide fuel cell performance and reactant concentration distributions depend on the flow field and mass transfer characteristics. The design of SOFC with a high output power density requires an understanding of the convective and diffusive mass transfer mechanism inside the flow channels and porous electrodes. Proper flow control is necessary to enhance the mass transfer and electrochemical reactions in SOFC. This section first presents and discusses the working mechanism of the radial flow and then analyzes the influence of the geometric parameters of the convergent conical ring inserts on the performance of the tubular SOFC.

#### 3.1. Influence of Radial Flows on the Performance of SOFC

We selected one representative case to analyze the effect of the insert structure on the flow and mass transfer characteristics in the tubular SOFC. The influence of the radial flow on the velocity field and mass transfer characteristics in tubular SOFCs is illustrated in Figure 4, which compares the predicted streamlines and hydrogen concentration distribution in the fuel channels and anode pores for the tubular SOFCs with and without an insert.

In the case of SOFC without inserts, the projected streamlines in the anode fuel channel are nearly parallel to the interface between the anode and fuel channel along the axial directions. In contrast, the predicted streamlines in the porous anode are oriented in the radial directions, indicating that diffusive behavior is dominant. The streamlines in the tubular SOFC with an insert show that the flow field is significantly affected by the insert structure, as illustrated by the wavy patterns inside the fuel channel and anode pores. These wavy patterns result from the placement of the insert inside the fuel channel, which partially blocks the flow path and forces the fuel to enter and travel inside the anode pores.

It is worth mentioning that the width of the insert structure,  $r_w$ , is crucial in determining the fuel's traveling distance inside the anodes.

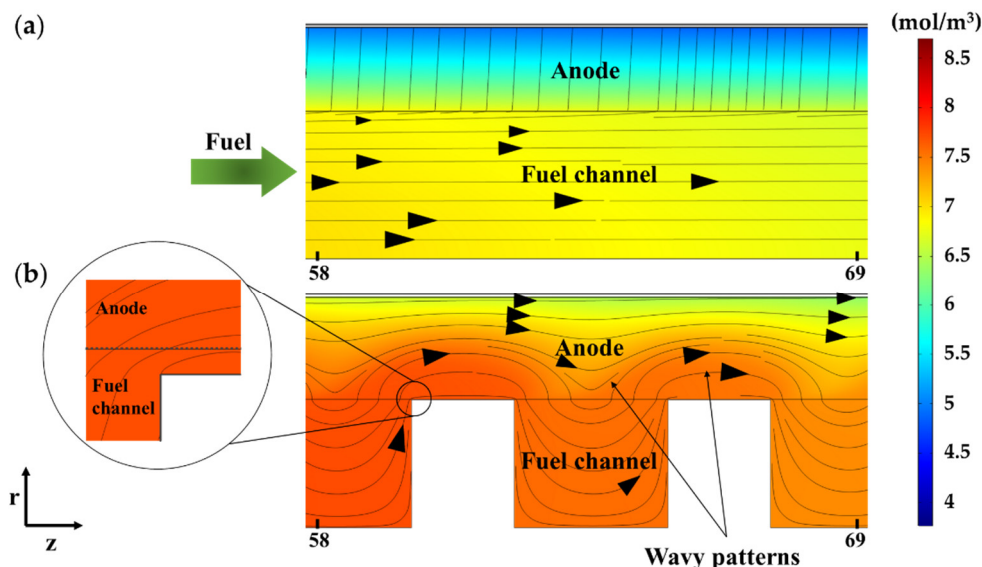


**Figure 4.** The predicted streamlines and H<sub>2</sub> molar concentrations in the fuel channels and anodes of tubular SOFCs with (a) no insert and (b) a convergent conical ring insert (the offset angle is 0 degrees).

The influence of radial flows on the hydrogen concentration distributions is also shown in Figure 4. The results show that the insert structure contributes to the increase in the local hydrogen concentration inside the anode pores. We compared the hydrogen concentrations in SOFC with and without an insert at identical axial locations. The local hydrogen concentration in SOFC with a conical ring insert is overall higher than that in the conventional tubular SOFC, as illustrated in Figure 4. The hydrogen concentration also exhibits a wavy distribution due to the existence of the conical ring inserts.

In order to quantitatively characterize the effect of the radial flows caused by the insert, we used the vorticity of the fuel at the interface between the fuel channel and anode to quantify the flow rotation, which can be expressed as:

$$\omega = \frac{\partial u_z}{\partial r} - \frac{\partial u_r}{\partial z} \tag{29}$$

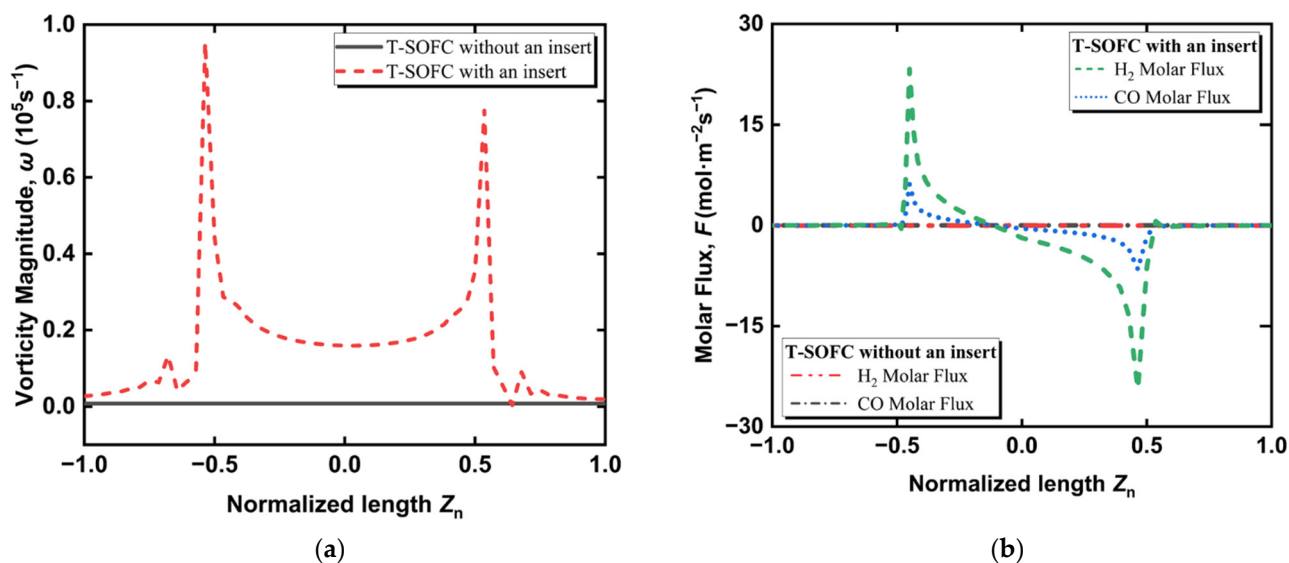
where  $\mathbf{u}$  is the velocity and the subscripts  $r$  and  $z$  denote the radial and axial velocity.

Figure 5a compares the vorticity distribution as a function of the normalized length,  $Z_n$ , at the anode/channel interface. The normalized length,  $Z_n$ , is given as:

$$Z_n = \frac{Z - Z_0}{r_w} \tag{30}$$

where  $r_w$  is the top width of the conical ring, as illustrated in Figure 1.  $Z$  and  $Z_0$  denote the axial positions and the center of the conical ring insert, respectively.

Figure 5a shows the distribution of the vorticity magnitude at the anode/channel interface in the tubular SOFC with a convergent conical ring insert at a zero-degree offset angle. The vorticity magnitude,  $\omega$ , exhibits two peaks with an order of magnitude of  $10^5 \text{ s}^{-1}$  in the case of SOFC with an insert. This high absolute value of the vorticity magnitude indicates that the convergent conical ring insert directs and facilitates more fuel to enter and leave the porous anode. The highest vorticity values appear at the top edges of the conical ring inserts. In contrast, there is no visible variation in the vorticity distribution in the conventional tubular SOFC.



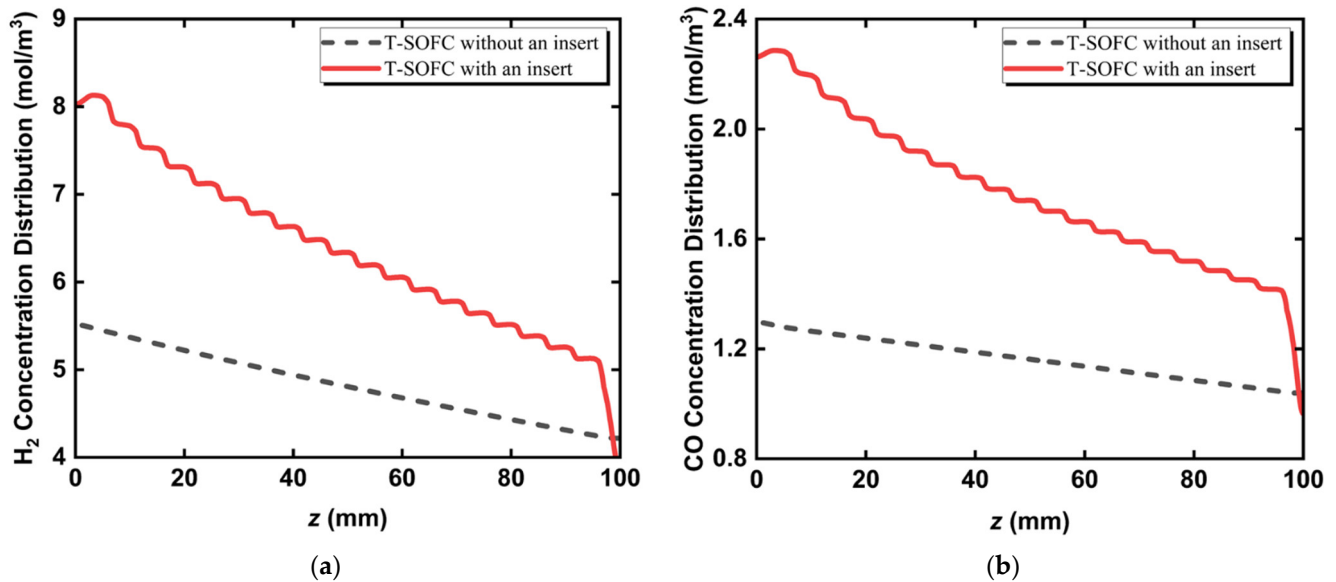
**Figure 5.** The axial distribution of (a) the vorticity magnitude and (b) normal molar fluxes of CO and  $\text{H}_2$  at the anode/channel interface for tubular SOFCs with and without inserts.

Figure 5b shows the effect of the generated vorticity on the mass transfer at the interface between the anode and fuel channel. It indicates that the normal molar flux of fuel in the conventional SOFC shows a minor variation while that in the case with inserts shows two peaks. The first peak indicates the fuel gas entering the anode, and the second peak indicates the fuel gas leaving the anode. The carbon monoxide and hydrogen show a similar trend, with peaks with maximum values of  $28.8$  ( $\text{mol}\cdot\text{m}^{-2}\cdot\text{s}^{-1}$ ) for  $\text{H}_2$  and  $7.2$  ( $\text{mol}\cdot\text{m}^{-2}\cdot\text{s}^{-1}$ ) for CO, respectively. The higher value of the hydrogen molar flux is mainly due to the high inlet molar fraction of hydrogen compared to that of carbon monoxide. Compared to the case without an insert, the peaks in the insert case reflect an increase in the convective molar flux, which means more fuel enters the porous anode.

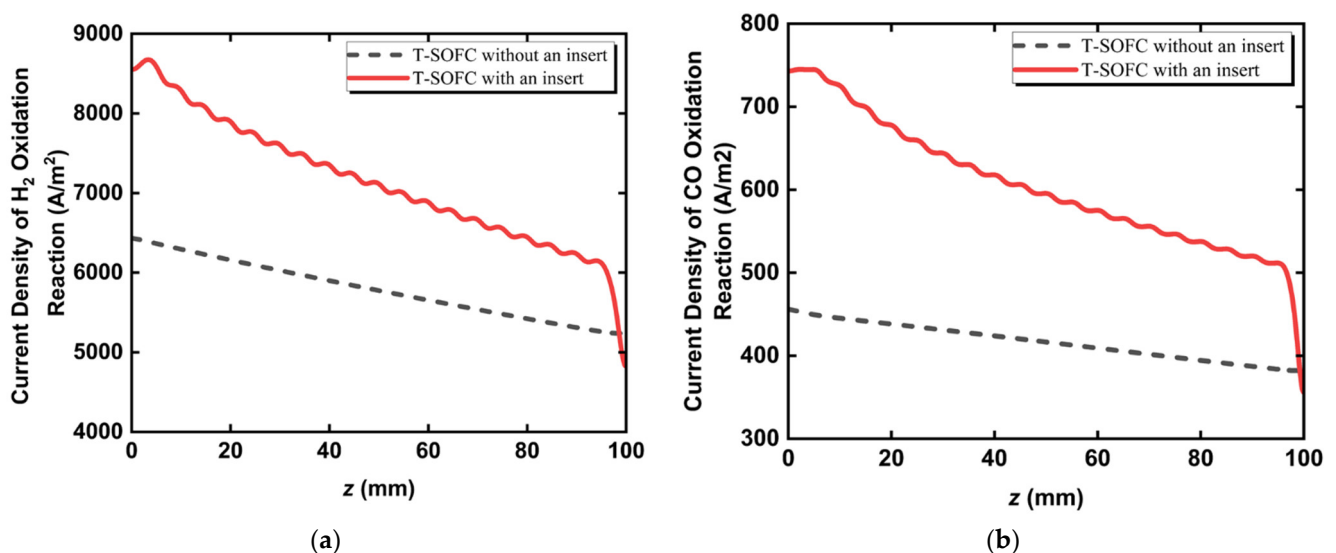
Figure 6 compares the axial hydrogen and carbon monoxide concentration distributions at the interface between the reaction and diffusion layers in SOFCs with and without inserts. The influence of the radial flows caused by the inserts on the axial  $\text{H}_2$  and CO concentration distributions for the electrochemical reactions are reflected in Figure 6. The local hydrogen concentration near the inlet is increased by approximately 1.5 times, indicating that the radial flows enhance the diffusive mass transfer in the anode and enable more hydrogen to reach the reaction layer. A similar trend can also be seen in the axial CO concentration distribution. The wavy axial  $\text{H}_2$  and CO concentration distributions in the case with an insert are mainly due to the flow field caused by placing the insert inside the fuel channel. It should also be noted that the hydrogen concentration is around 3.5 times larger than the carbon monoxide concentration due to a higher inlet hydrogen mole fraction.

Figure 7 illustrates the effect of mass transfer enhancement on the electrochemical reactions of SOFC. It compares the local current densities from the  $\text{H}_2$  and CO oxidation reactions as a function of the axial positions at the interface between the reaction layer and the diffusion layer for SOFC with and without the insert. The current density distribution shows a similar trend to the concentration distribution. Figure 7 shows that the contribution of electrochemical reactions from hydrogen to the local current density is around one order of magnitude higher than that from carbon monoxide. The increase in the local current densities is due to the insert structure increasing the radial convective mass transfer, which drives more fuel to the triple-phase boundaries, improving the electrochemical reaction rates and therefore increasing the local current densities of SOFC. It also indicates that the placement of an insert structure inside the fuel channel can potentially increase the local current densities compared to the no insert case. In the case with an insert, the local

current density shows a maximum increase of approximately 35% near the inlet compared to the no insert case. These results are consistent with the findings shown in Figure 6. By integrating the current density along the  $z$ -direction, we could calculate the total output current of SOFC with and without inserts. We found that placing the insert inside the fuel channel could increase the overall current density by 19.14% compared to the conventional tubular SOFC.



**Figure 6.** The axial concentration distributions of (a) hydrogen and (b) carbon monoxide at the interface between the reaction and diffusion layers in tubular SOFCs with and without inserts.



**Figure 7.** The axial distribution of current densities from (a) hydrogen electrochemical oxidation and (b) carbon monoxide electrochemical oxidation at the interface between the reaction and diffusion layers in tubular SOFCs with and without inserts.

In order to characterize the influence of the insert structure and establish a link between the electrochemical reactions and mass transfer performance inside the porous anode, we defined the local Péclet number and the mass transfer conductance for the examined cases in this study as follows.

The local Péclet number,  $Pe$ , is defined as the ratio of convection to diffusion, which can be calculated from Equation (31):

$$Pe_i = \frac{|u_r|r_p}{D_{i,eff}} \quad (31)$$

where  $u_r$  is the radial velocity and  $r_p$  is the effective pore radius. The effective diffusion coefficient of the gas species  $i$  is denoted by  $D_{i,eff}$  and expressed as follows:

$$D_{i,eff} = \frac{1-x_i}{\sum_{i \neq j} x_j / D_{ij,eff}} \quad (32)$$

The mass transfer conductance of the gas component  $i$ ,  $g_{m,i}$  is defined as Equation (33), which evaluates the ability of a gas component to migrate inside the porous electrode:

$$g_{m,i} = \frac{J_{net}}{(m_{i,d} - m_{i,e})_{ave}} \quad (33)$$

where  $J_{net}$  is the normal total flux and  $m_i$  is the average mass fraction of species  $i$ . The subscript  $i$  represents different gas components.  $d$  denotes the interface between the anode and fuel channel and  $e$  denotes the interface between the reaction and diffusion layers.

Figure 8 compares the local Péclet numbers as a function of the normalized length at the anode/fuel channel interface for tubular SOFCs with and without the conical ring insert. The zero position in the  $x$ -axis denotes the center of a conical ring insert while the locations of 0.5 and  $-0.5$ , respectively, represent the corners of the chosen conical ring. The local Péclet numbers in the conventional tubular SOFC are on the order of magnitude of  $10^{-5}$  for both CO and H<sub>2</sub> and show trivial variations. In contrast, the local Péclet numbers near the insert corners exhibit two peaks on the order of magnitude of  $10^{-3}$ . It should also be noted that the maximum Péclet number of carbon monoxide is 25% higher than that of hydrogen. This is because hydrogen diffusion in the porous anode is easier than carbon monoxide due to its small molecular size.

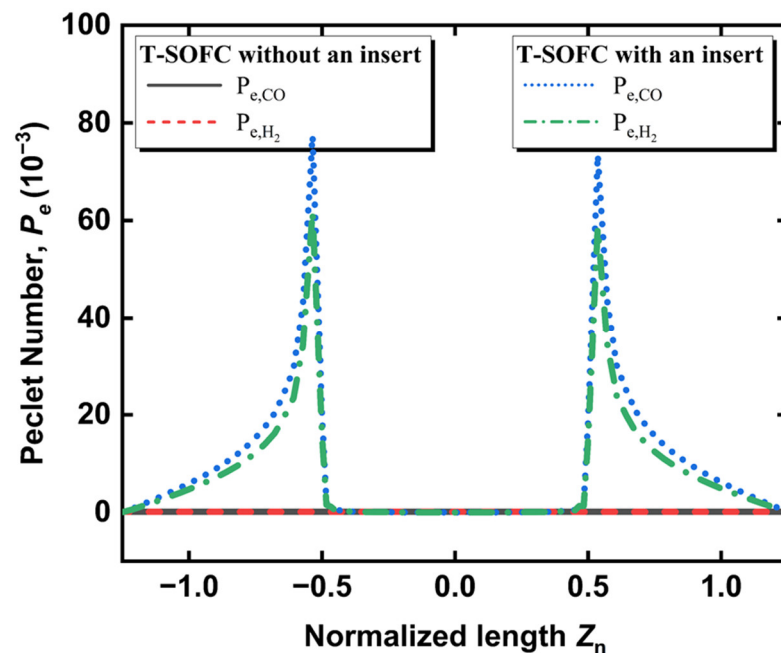


**Figure 8.** The axial distribution of Péclet numbers at the anode/channel interface in the tubular SOFCs with and without inserts.

Figure 9a compares the mass transfer conductance of H<sub>2</sub> and CO in tubular SOFCs with and without the conical ring insert. It shows that the mass transfer conductance is significantly increased due to the radial flows, which roughly doubles the mass transfer con-

ductance of hydrogen and increases that of carbon monoxide by three times. The increase in the radial convective mass transfer significantly enhances the reactant concentration near the gas diffusion layer, increasing the electrochemical reactions and improving the overall performance of SOFC. As a result, the  $H_2$  mass transfer conductance rate increased from about  $1.5 \times 10^{-3}$  to  $3 \times 10^{-3}$  while the CO mass transfer conductance rate increased from  $0.5 \times 10^{-3}$  to  $1.5 \times 10^{-3}$ . The overall output power improvement in the tubular SOFC with and without an insert is shown in Figure 9b. When compared to the no insert case, the conical ring insert has the potential to increase the overall output power of SOFC by 19.14%.

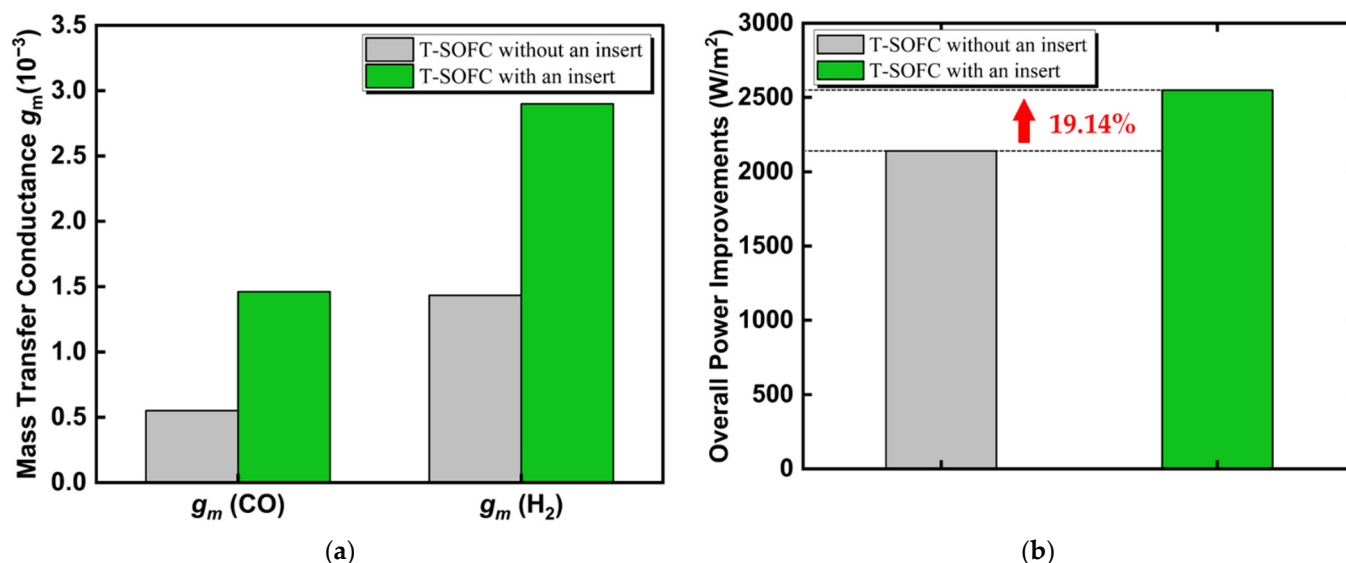


**Figure 9.** Comparison of (a) the mass transfer conductance and (b) the power densities in tubular SOFCs with and without inserts.

### 3.2. Effect of the Conical Ring Radius

The effects of the different geometric parameters on the electrochemical performance of the tubular SOFC were then investigated. We first examined the influence of the conical ring insert radii, which varied from 3.25 to 3.49 mm with a step of 0.01 mm. In this section, the offset angle,  $\alpha$ , was fixed as  $0^\circ$ , as illustrated in Figure 1 (i.e., the width of the ribs,  $r_w$ , is 2 mm).

Figure 10a shows the vorticity magnitude as a function of the normalized length at the anode/channel interface for three cases with different radii. It indicates that increasing the radius of the conical ring inserts from 3.25 to 3.45 mm could approximately increase the highest vorticity magnitude values from  $10^5$  to  $2.5 \times 10^5 \text{ s}^{-1}$  at the ring edges. As the insert radii increase, the gap between the conical ring inserts and the anode/channel interface decreases. The flow resistance between the conical ring inserts and the anode/channel interface is significantly increased, facilitating more fuel to enter the porous anode instead of traveling through the small gap. This increases the radial velocity of fuel and therefore increases the peak vorticity magnitude. As illustrated in Figure 10b, the maximum radial velocity is increased from 0.18 to 3.42 m/s as the insert radii are increased from 3.25 to 3.49 mm, which could effectively promote the fuel transport from the channel to the porous anode.

It is also interesting to note that the vorticity distribution for the case with the insert radii of 3.45 mm differs from the other two cases. This is due in part to the fact that the small gap increases the flow resistance of the narrow region between the insert and the anode, which prevents the fuel from traveling through the anode/channel interface.

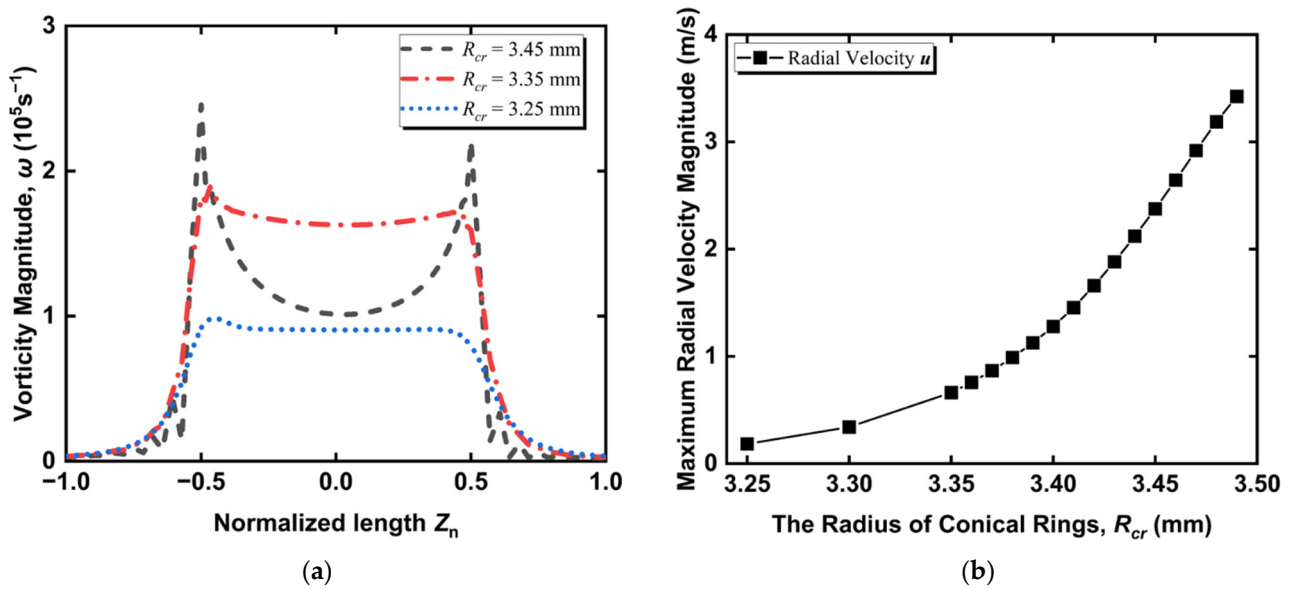


**Figure 10.** The influence of the conical ring radius on (a) the vorticity magnitude distributions and (b) maximum radial velocity magnitude.

The effect of the conical ring radius variation on the electrochemical reactions could be reflected by the output power of the tubular SOFC. We defined a net output power improvement,  $P_{in,net}$ , as follows:

$$P_{in,net} = P_{in} - P_{Pump} \quad (34)$$

where the total output power of the tubular SOFC with inserts is represented by  $P_{in}$  and the pump power required to sustain the flow is denoted by  $P_{pump}$ , which can be calculated as:

$$P_{Pump} = \frac{\Delta P \cdot \dot{m}_{fuel}}{\rho} \quad (35)$$

where  $\Delta P$  denotes the gas-phase pressure drop calculated from the pressure difference between the inlet and outlet of the fuel channels.  $\dot{m}_{fuel}$  and  $\rho$ , respectively, represent the mass flow rate and density of the fuel. We also used the percentage of the net power improvement to compare the performance of the tubular SOFC with and without inserts. The  $P_{no,net}$  is the net output power of the conventional tubular SOFC (i.e., the tubular SOFC without inserts):

$$P_{net} \% = 100\% \times \frac{(P_{in,net} - P_{no,net})}{P_{no,net}} \quad (36)$$

Figure 11 shows the effect of the conical ring radius variation on the net power improvements and the required pump power. The percentage of the net power and the pump power increase as the conical ring insert radii increase. This increase in the net power indicates that the enhanced electrochemical reaction could outweigh the frictional loss inside the porous anode. The maximum net power improvement in the examined cases reaches approximately 12% when the conical ring radii are around 3.49 mm. The pump power demands increased from 0.07 to 0.54 W as the radii increased from 3.25 to 3.49 mm. It is worth noting that the pump power demand is 7.8% higher for an overall power improvement of 19.14%. However, the net power improvements far outweigh the increase in pump power demands.

The net output power of the tubular SOFC is improved mainly by the radial flows, which enhance the convective mass transfer at the channel/anode interface and facilitate more fuel to enter the anode. Figure 12 shows the average mass transfer conductance as a function of the conical ring radius. As the conical ring insert radii increase, the mass transfer conductance of both hydrogen and carbon monoxide increases. The increased

radial velocity at the anode/channel interface could effectively promote the mass transfer in the porous anode as the conical ring insert radii are increased from 3.25 to 3.49 mm. The mass transfer conductance of both hydrogen and carbon monoxide is approximately doubled. Figure 12b shows the total consumption rates of hydrogen and carbon monoxide in the tubular SOFC. For a fixed conical ring insert radius, the mass consumption rate of hydrogen at the triple-phase boundaries is comparable to that of carbon monoxide. Since the molecular weight of hydrogen is 14 times smaller than that of carbon monoxide, the current produced from hydrogen oxidation is approximately 15 times larger than that from the oxidation of carbon monoxide. We show that increasing the conical ring insert radii from 3.25 to 3.49 mm could increase the H<sub>2</sub> and CO consumption by approximately 13% and 39%, respectively.

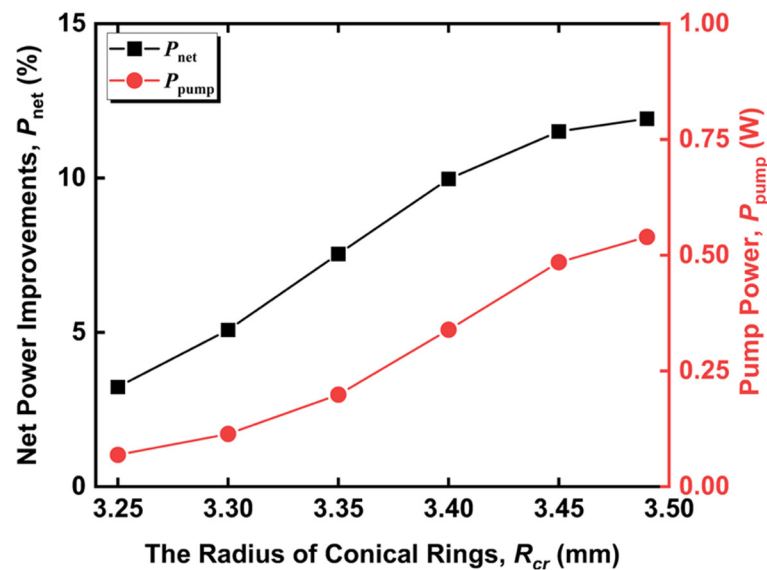


Figure 11. The percentage of the net power improvement and the required pump power as a function of the conical ring radius.

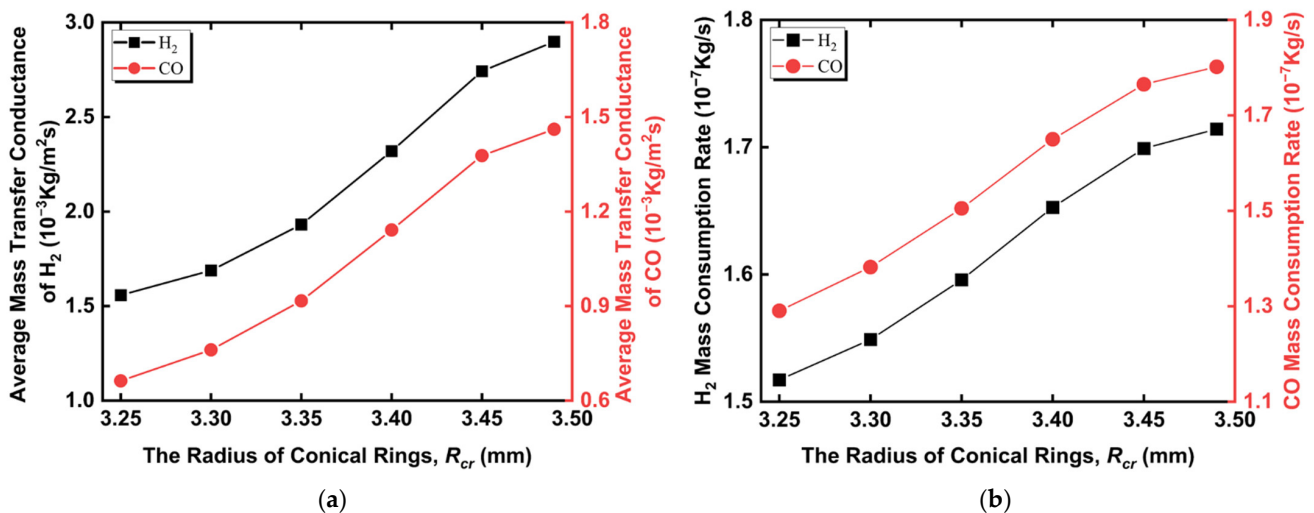
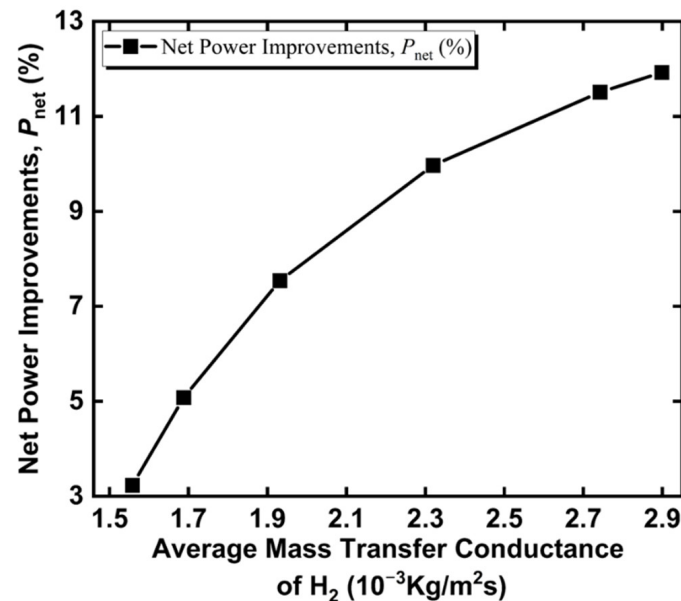


Figure 12. The effects of the conical ring radius on (a) the mass transfer conductance and (b) the fuel mass consumption rates.

We plotted the relationship between the mass transfer conductance and the net power improvement to link the electrochemical reaction with the mass transfer characteristics. Since the electrochemical reaction fueled by hydrogen dominates, we only plotted the

mass transfer conductance of hydrogen. Figure 13 shows that the net power improvement is proportional to the mass transfer conductance. As the mass transfer conductance is increased from  $1.5 \times 10^{-3}$  to  $2.5 \times 10^{-3}$   $\text{kg}/(\text{m}^2\text{s})$ , the net power improvement is increased by approximately 4 times. The mass transfer conductance is increased because of the high radial velocity. A further increase in the mass transfer conductance of hydrogen shows a negligible impact on the electrochemical reaction in the examined cases. This emphasizes the importance of mass transfer conductance for the fuel channel design. A higher-output-power tubular SFOC requires the design of the fuel channel to have a large mass transfer conductance.



**Figure 13.** The percentage of the net power improvements as a function of the average mass transfer conductance of H<sub>2</sub>.

### 3.3. Effect of the Conical Ring Offset Angle

We then investigated the effect of the offset angle variation on the performance of tubular SOFCs. The offset angle examined in this section ranged from  $0^\circ$  to  $21^\circ$  while the radius of the conical ring inserts was fixed as 3.49 mm. Since the base of the conical ring inserts is unchanged, the offset angle variations only affect the top width of the insert rib, which is only 0.1 mm at an offset angle of  $21^\circ$ . We should note that 0.1 mm is the smallest width we can choose for the convergent conical ring insert.

Figure 14a shows the vorticity magnitude as a function of the normalized length. It should be noted that the top widths of the conical ring inserts are different for various offset angles. As the offset angle is increased from  $0^\circ$  to  $21^\circ$ , the maximum vorticity magnitude gradually increases due to the increase in the fuel radial velocity, as illustrated in Figure 14b. The increase in the maximum radial velocity is in part due to the decrease in the flow resistance as the tip of the conical ring becomes sharper. The low flow resistance also facilitates the fuel to enter or leave the anode in the region between the conical rings and the anode, which increases the vorticity magnitudes between the ring edges. Figure 14a also shows that the distance between two vorticity peaks gradually decreases with the increasing offset angle. This is due in part to the fact that the axial velocity component gradually increases as the offset angle increases, as illustrated in Figure 14b. The location of the maximum velocity and the maximum vorticity thereby gradually deviate from the conical ring edges.

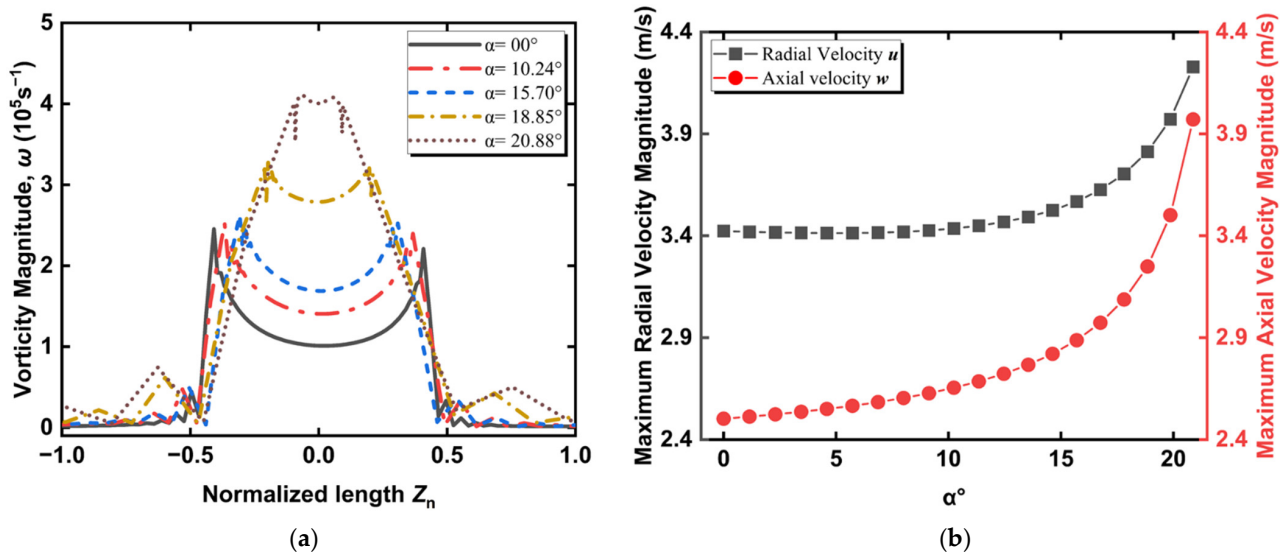


Figure 14. The influence of the offset angle on: (a) the vorticity magnitude and (b) maximum radial and axial velocity magnitude.

Figure 15 shows the effect of the offset angle variation on the net power improvements and pump power demands. It indicates that increasing the offset angle from  $0^\circ$  to  $21^\circ$  could slightly reduce the net power improvement by approximately 2%. This implies that the radius of the conical ring is the primary factor determining the improvement of the electrochemical reactions. However, the pump power is significantly reduced. Increasing the offset angle from  $0^\circ$  to  $21^\circ$  resulted in a 42% reduction in the required pump power due to the reduction in frictional losses in the narrow region between the insert and the anode. The frictional loss of the gas mixture in the porous anode is also reduced since the gas traveling distance in the porous anode becomes shorter with the increasing angles. These findings imply that the design of a conical ring insert with a larger radius and offset angle could achieve a high output power while requiring less pump power.

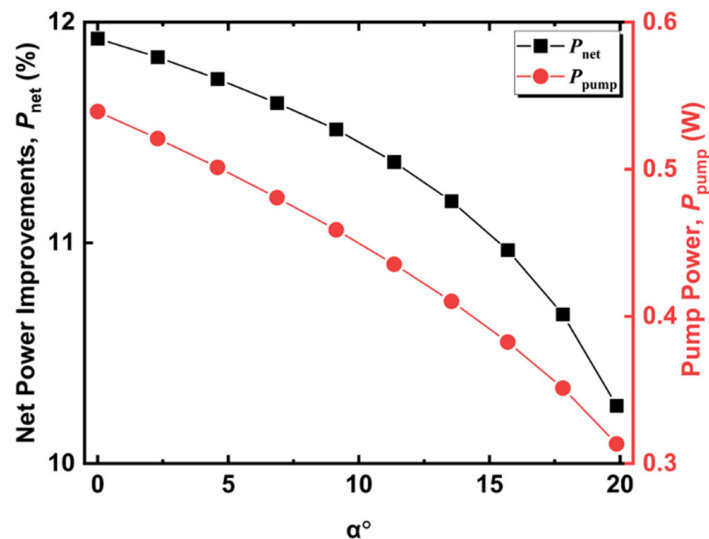
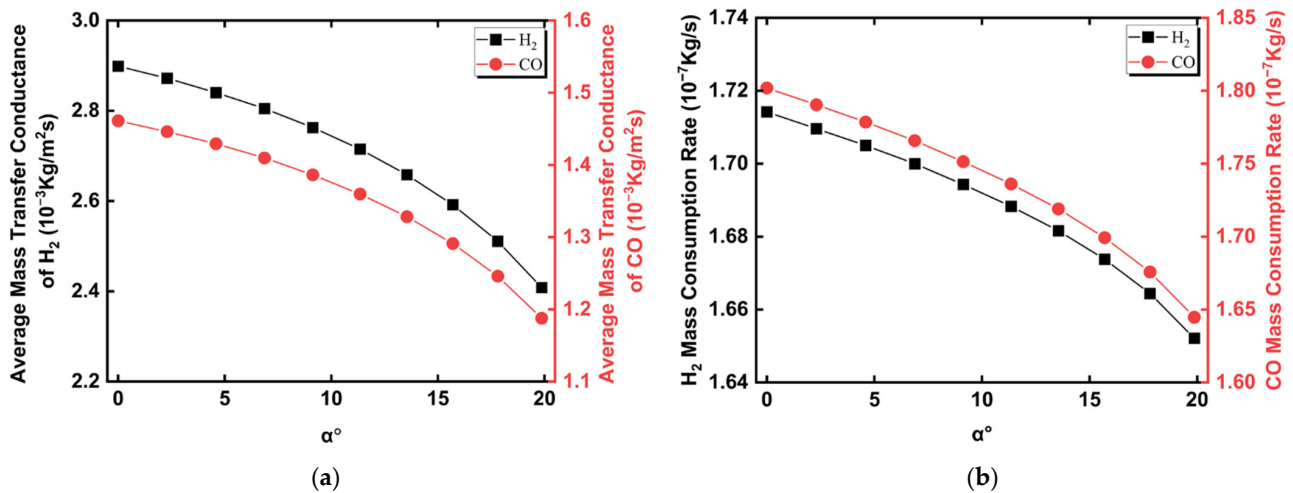


Figure 15. The percentage of the net power improvement and the required pump power as a function of the conical ring offset angle.

The relationship between the mass transfer conductance and the offset angle is illustrated in Figure 16. The mass transfer conductance slightly decreases as the offset angle increases. As the offset angle decreases, the width of the conical ring inserts increases,

forcing the fuel to travel a longer distance before leaving the anode, which consequently increases the mass transfer conductance rate. The average mass transfer conductance of hydrogen could be increased from  $2.4 \times 10^{-3}$  to  $2.9 \times 10^{-3}$  kg/(m<sup>2</sup>s) as the offset angle decreases from 21° to 0°. Figure 16b shows that the consumption rate also exhibits the same trend as the mass transfer conductance. The variation of the fuel consumption is within 10% for all the offset angles examined in our study. This indicates that the offset angle is not a primary factor affecting the electrochemical reactions.



**Figure 16.** The effect of the conical ring offset angle on: (a) the mass transfer conductance and (b) the fuel consumption rates.

Figure 17 represents the relationship between the average mass transfer conductance and the percentage of net power density improvements. It shows that the net power improvement is proportional to the mass transfer conductance. The increase in the mass transfer conductance rate is a consequence of the increase in the radial velocities, as illustrated in Figure 14b. As the mass transfer conductance increases from  $2.4 \times 10^{-3}$  to  $2.9 \times 10^{-3}$  kg/(m<sup>2</sup>s), the output power of the tubular SOFC is improved by 1.7%. This is consistent with the results in Figure 13 and further emphasizes the strong relationship between the mass transfer conductance and net output power improvements.

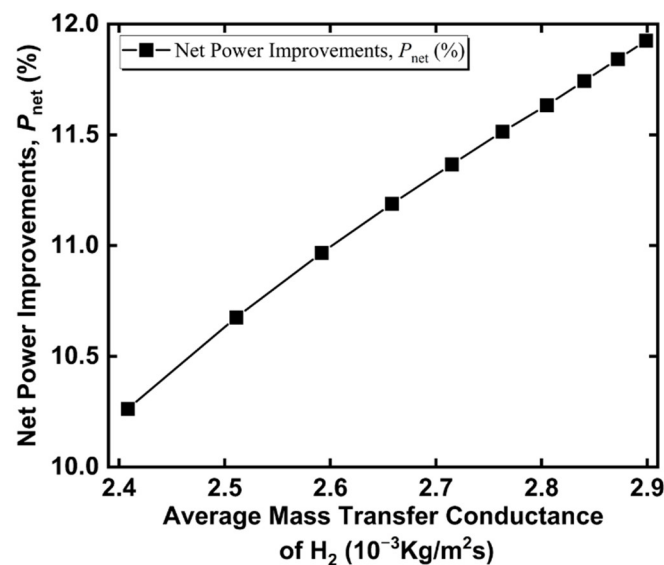


**Figure 17.** The percentage of the net power density improvements as a function of the average mass transfer conductance of H<sub>2</sub>.

#### 4. Conclusions

This paper investigated the influence of the radial flows generated by the convergent conical ring insert on the mass transfer characteristics and electrochemical reactions of the tubular SOFC. The radial flow could improve the fuel diffusion within the porous electrode to reach the diffusion layer and increase the local fuel concentrations. Increasing the local fuel concentration inside the porous electrode could effectively enhance the electrochemical reaction and increase the power density. We demonstrated that the tubular SOFC could achieve an overall power density of 19.14% by placing the convergent conical ring insert in the fuel channel.

The effects of the conical ring radius and offset angle on the net power density and gas-phase pressure drop of the tubular SOFC were also examined. We proposed the mass transfer conductance of fuel to quantify the performance of the convergent conical ring inserts on tubular SOFC net power improvements, since the net power improvement of the tubular SOFC is proportional to the fuel's average mass transfer conductance.

We demonstrated that increasing the conical ring radius to 3.49 mm could enhance the mass transfer conductance and increase the net power improvement percentage by approximately 12%. In contrast, the offset angle of the insert has a negligible impact on the fuel mass transfer conductance. The power density is primarily affected by the radius of the conical ring insert while the offset angle is crucial in reducing the frictional losses in the narrow region between the insert and the anode. We showed that increasing the offset angle from 0° to 21° could reduce the pump power demands by 42% at a 1.7% reduction in the net power improvement.

It is suggested that in order to develop a high-power-density tubular SOFC that requires less pump power, a convergent conical ring insert with a larger radius and a larger offset angle should be designed. This study outlined the importance of radial flows and mass transfer conductance in improving the design and performance of tubular SOFCs, aiming to increase the net power density of this technology and reduce frictional losses to meet the vehicle power requirements.

**Author Contributions:** Conceptualization, A.E. and Z.Z.; Data curation, A.E., Z.Z. and B.Z.; Formal analysis, A.E. and Z.Z.; Funding acquisition, Y.Q., W.Z. and Y.Z.; Investigation, A.E.; Methodology, A.E., Z.Z. and Y.Z.; Project administration, Y.Q., W.Z. and Y.Z.; Resources, Y.Q., W.Z. and Y.Z.; Software, A.E. and B.Z.; Supervision, Z.Z. and Y.Z.; Validation, A.E. and C.H.; Visualization, A.E. and Z.Z.; Writing—original draft, A.E.; Writing—review & editing, A.E., Z.Z., B.Z. and Y.Z. All authors have read and agreed to the published version of the manuscript.

**Funding:** The present article is based on work supported in part by The Advanced Aviation Power Innovation institution and The Aero Engine Academy of China and supported by Tsinghua University Initiative Scientific Research Program.

**Data Availability Statement:** Not applicable.

**Conflicts of Interest:** The authors declare no conflict of interest. The funders had no role in the design of the study; in the collection, analyses, or interpretation of data; in the writing of the manuscript; or in the decision to publish the results.

#### References

1. Fernandes, A.; Woudstra, T.; van Wijk, A.; Verhoef, L.; Aravind, P.V. Fuel Cell Electric Vehicle as a Power Plant and SOFC as a Natural Gas Reformer: An Exergy Analysis of Different System Designs. *Appl. Energy* **2016**, *173*, 13–28. [[CrossRef](#)]
2. Luo, Y.; Shi, Y.; Cai, N. Chapter 4—High-Efficiency Hybrid Fuel Cell Systems for Vehicles and Micro-CHPs. In *Hybrid Systems and Multi-Energy Networks for the Future Energy Internet*; Academic Press: Cambridge, MA, USA, 2021; pp. 85–111. [[CrossRef](#)]
3. Bessekon, Y.; Zielke, P.; Wulff, A.C.; Hagen, A. Simulation of a SOFC/Battery Powered Vehicle. *Int. J. Hydrog. Energy* **2019**, *44*, 1905–1918. [[CrossRef](#)]
4. O'Hayre, R.P.; Cha, S.-W.; Colella, W.G.; Prinz, F.B. *Fuel Cell Fundamentals*, 3rd ed.; John Wiley & Sons Inc.: Hoboken, NJ, USA, 2016; ISBN 978-1-119-11415-4.
5. Zeng, Z.; Qian, Y.; Zhang, Y.; Hao, C.; Dan, D.; Zhuge, W. A Review of Heat Transfer and Thermal Management Methods for Temperature Gradient Reduction in Solid Oxide Fuel Cell (SOFC) Stacks. *Appl. Energy* **2020**, *280*, 115899. [[CrossRef](#)]

6. Cimen, F.M.; Kumuk, B.; Ilbas, M. Simulation of Hydrogen and Coal Gas Fueled Flat-Tubular Solid Oxide Fuel Cell (FT-SOFC). *Int. J. Hydrog. Energy* **2022**, *47*, 3429–3436. [[CrossRef](#)]
7. Sallam, E.R.; Khairy, H.M.; Elnouby, M.S.; Fetouh, H.A. Sustainable Electricity Production from Seawater Using Spirulina Platensis Microbial Fuel Cell Catalyzed by Silver Nanoparticles-Activated Carbon Composite Prepared by a New Modified Photolysis Method. *Biomass Bioenergy* **2021**, *148*, 106038. [[CrossRef](#)]
8. Santarelli, M.; Cabrera, M.; Cali, M. Solid Oxide Fuel Based Auxiliary Power Unit for Regional Jets: Design and Mission Simulation with Different Cell Geometries. *J. Fuel Cell Sci. Technol.* **2010**, *7*, 021006. [[CrossRef](#)]
9. Sallam, E.R.; Khairy, H.M.; Elshobary, M.; Fetouh, H.A. *Application of Algae for Hydrogen Generation and Utilization: In Practice, Progress, and Proficiency in Sustainability*; El-Sheekh, M.M., Abdullah, N., Ahmad, I., Eds.; IGI Global: Hershey, PA, USA, 2022; pp. 354–378. ISBN 978-1-66842-438-4.
10. Sallam, E.R.; Fetouh, H.A. Comparative Study for the Production of Sustainable Electricity from Marine Sediment Using Recyclable Low-Cost Solid Wastes Aluminum Foil and Graphite Anodes. *ChemistrySelect* **2022**, *7*, e202103972. [[CrossRef](#)]
11. Kong, W.; Han, Z.; Lu, S.; Gao, X.; Wang, X. A Novel Interconnector Design of SOFC. *Int. J. Hydrog. Energy* **2020**, *45*, 20329–20338. [[CrossRef](#)]
12. Kendall, K. Progress in Microtubular Solid Oxide Fuel Cells. *Int. J. Appl. Ceram. Technol.* **2010**, *7*, 1–9. [[CrossRef](#)]
13. Mukerjee, S.; Leah, R.; Selby, M.; Stevenson, G.; Brandon, N.P. Life and Reliability of Solid Oxide Fuel Cell-Based Products. In *Solid Oxide Fuel Cell Lifetime and Reliability*; Elsevier: Amsterdam, The Netherlands, 2017; pp. 173–191. ISBN 978-0-08-101102-7.
14. Leah, R.T.; Bone, A.; Hammer, E.; Selcuk, A.; Rahman, M.; Clare, A.; Mukerjee, S.; Selby, M. Development Progress on the Ceres Power Steel Cell Technology Platform: Further Progress Towards Commercialization. *ECS Trans.* **2017**, *78*, 87–95. [[CrossRef](#)]
15. Matus, Y.; Dejonghe, L.; Jacobson, C.; Visco, S. Metal-Supported Solid Oxide Fuel Cell Membranes for Rapid Thermal Cycling. *Solid State Ion.* **2005**, *176*, 443–449. [[CrossRef](#)]
16. Kendall, K.; Dikwal, C.M.; Bujalski, W. Comparative Analysis of Thermal and Redox Cycling for Microtubular SOFCs. *ECS Trans.* **2019**, *7*, 1521–1526. [[CrossRef](#)]
17. Campana, R.; Merino, R.I.; Larrea, A.; Villarreal, I.; Orera, V.M. Fabrication, Electrochemical Characterization and Thermal Cycling of Anode Supported Microtubular Solid Oxide Fuel Cells. *J. Power Sources* **2009**, *192*, 120–125. [[CrossRef](#)]
18. Cable, T.L.; Sofie, S.W. A Symmetrical, Planar SOFC Design for NASA's High Specific Power Density Requirements. *J. Power Sources* **2007**, *174*, 221–227. [[CrossRef](#)]
19. Yuan, H. *Compare New Designed Flow Channels of Interconnect for Planar SOFCs with Typical Channels*; Department of Energy Sciences, Faculty of Engineering, Lund University: Lund, Sweden, 2009; p. 7.
20. Danilov, V.A.; Tade, M.O. A CFD-Based Model of a Planar SOFC for Anode Flow Field Design. *Int. J. Hydrog. Energy* **2009**, *34*, 8998–9006. [[CrossRef](#)]
21. Saied, M.; Ahmed, K.; Nemat-Alla, M.; Ahmed, M.; El-Sebaie, M. Performance Study of Solid Oxide Fuel Cell with Various Flow Field Designs: Numerical Study. *Int. J. Hydrog. Energy* **2018**, *43*, 20931–20946. [[CrossRef](#)]
22. Yu, Z.; Xu, Y.; Hu, B.; Liu, S.; Zhang, X. Comparing the Air Flow Distribution Qualities Among Three Different Air Flow Path Configurations for Tubular Solid Oxide Fuel Cell Stacks. *Int. J. Electrochem. Sci.* **2016**, *11*, 9100–9109. [[CrossRef](#)]
23. Chen, D.; Xu, Y.; Hu, B.; Yan, C.; Lu, L. Investigation of Proper External Air Flow Path for Tubular Fuel Cell Stacks with an Anode Support Feature. *Energy Convers. Manag.* **2018**, *171*, 807–814. [[CrossRef](#)]
24. Khazaei, I.; Rava, A. Numerical Simulation of the Performance of Solid Oxide Fuel Cell with Different Flow Channel Geometries. *Energy* **2017**, *119*, 235–244. [[CrossRef](#)]
25. Huang, H.; Han, Z.; Lu, S.; Kong, W.; Wu, J.; Wang, X. The Analysis of Structure Parameters of MOLB Type Solid Oxide Fuel Cell. *Int. J. Hydrog. Energy* **2020**, *45*, 20351–20359. [[CrossRef](#)]
26. Fu, Q.; Li, Z.; Wei, W.; Liu, F.; Xu, X.; Liu, Z. Performance Enhancement of a Beam and Slot Interconnector for Anode-Supported SOFC Stack. *Energy Convers. Manag.* **2021**, *241*, 114277. [[CrossRef](#)]
27. Bhattacharya, D.; Mukhopadhyay, J.; Biswas, N.; Basu, R.N.; Das, P.K. Performance Evaluation of Different Bipolar Plate Designs of 3D Planar Anode-Supported SOFCs. *Int. J. Heat Mass Transf.* **2018**, *123*, 382–396. [[CrossRef](#)]
28. Guo, A.-N.; Wang, L.-B. Parametrization of Secondary Flow Intensity for Laminar Forced Convection in Twisted Elliptical Tube and Derivation of Loss Coefficient and Nusselt Number Correlations by Numerical Analysis. *Int. J. Therm. Sci.* **2020**, *155*, 106425. [[CrossRef](#)]
29. Wei, S.-S.; Wang, T.-H.; Wu, J.-S. Numerical Modeling of Interconnect Flow Channel Design and Thermal Stress Analysis of a Planar Anode-Supported Solid Oxide Fuel Cell Stack. *Energy* **2014**, *69*, 553–561. [[CrossRef](#)]
30. Canavar, M.; Mat, A.; Celik, S.; Timurkutluk, B.; Kaplan, Y. Investigation of Temperature Distribution and Performance of SOFC Short Stack with/without Machined Gas Channels. *Int. J. Hydrog. Energy* **2016**, *41*, 10030–10036. [[CrossRef](#)]
31. Zeng, Z.; Hao, C.; Zhao, B.; Qian, Y.; Zhuge, W.; Wang, Y.; Shi, Y.; Zhang, Y. Local Heat Transfer Enhancement by Recirculation Flows for Temperature Gradient Reduction in a Tubular SOFC. *Int. J. Green Energy* **2022**, *19*, 1132–1147. [[CrossRef](#)]
32. Essaghouri, A.; Zeng, Z.; Zhao, B.; Hao, C.; Qian, Y.; Zhuge, W.; Zhang, Y. Effects of Radial and Circumferential Flows on Power Density Improvements of Tubular Solid Oxide Fuel Cells. *Energies* **2022**, *15*, 7048. [[CrossRef](#)]
33. Zhao, B.; Zeng, Z.; Hao, C.; Essaghouri, A.; Qian, Y.; Zhuge, W.; Wang, Y.; Shi, Y.; Zhang, Y. A Study of Mass Transfer Characteristics of Secondary Flows in a Tubular Solid Oxide Fuel Cell for Power Density Improvement. *Int. J. Energy Res.* **2022**. [[CrossRef](#)]

34. Radaideh, M.I.; Radaideh, M.I. Efficient Analysis of Parametric Sensitivity and Uncertainty of Fuel Cell Models with Application to SOFC. *Int. J. Energy Res.* **2020**, *44*, 2517–2534. [[CrossRef](#)]
35. Ni, M. An Electrochemical Model for Syngas Production by Co-Electrolysis of H<sub>2</sub>O and CO<sub>2</sub>. *J. Power Sources* **2012**, *202*, 209–216. [[CrossRef](#)]
36. Wang, Y.; Ren, J.; Shi, Y.; Li, X. Numerical Model of Direct Internal Reforming SOFC: A Comparison between Anode-Support and Metal-Support. *ECS Trans.* **2019**, *91*, 2013–2022. [[CrossRef](#)]
37. Wesselingh, J.A.; Krishna, R.; Krishna, R. *Mass Transfer in Multicomponent Mixtures*, 1st ed.; VSSD: Delft, The Netherlands, 2006; ISBN 978-90-71301-58-2.
38. Nagata, S.; Momma, A.; Kato, T.; Kasuga, Y. Numerical Analysis of Output Characteristics of Tubular SOFC with Internal Reformer. *J. Power Sources* **2001**, *101*, 60–71. [[CrossRef](#)]
39. Mirahmadi, A.; Valefi, K. Study of Thermal Effects on the Performance of Micro-Tubular Solid-Oxide Fuel Cells. *Ionics* **2011**, *17*, 767–783. [[CrossRef](#)]
40. Chen, B.; Xu, H.; Tan, P.; Zhang, Y.; Xu, X.; Cai, W.; Chen, M.; Ni, M. Thermal Modelling of Ethanol-Fuelled Solid Oxide Fuel Cells. *Appl. Energy* **2019**, *237*, 476–486. [[CrossRef](#)]
41. Akhtar, N.; Decent, S.P.; Kendall, K. A Parametric Analysis of a Micro-Tubular, Single-Chamber Solid Oxide Fuel Cell (MT-SC-SOFC). *Int. J. Hydrog. Energy* **2011**, *36*, 765–772. [[CrossRef](#)]
42. Williford, R.E.; Chick, L.A.; Maupin, G.D.; Simner, S.P.; Stevenson, J.W. Diffusion Limitations in the Porous Anodes of SOFCs. *J. Electrochem. Soc.* **2003**, *150*, A1067. [[CrossRef](#)]
43. Chen, B.; Xu, H.; Ni, M. Modelling of SOEC-FT Reactor: Pressure Effects on Methanation Process. *Appl. Energy* **2017**, *185*, 814–824. [[CrossRef](#)]
44. Todd, B.; Young, J.B. Thermodynamic and Transport Properties of Gases for Use in Solid Oxide Fuel Cell Modelling. *J. Power Sources* **2002**, *110*, 186–200. [[CrossRef](#)]
45. Poling, B.E.; Prausnitz, J.M.; O'Connell, J.P. *The Properties of Gases and Liquids*, 5th ed.; McGraw-Hill: New York, NY, USA, 2001; ISBN 978-0-07-011682-5.
46. Ni, M. Computational Fluid Dynamics Modeling of a Solid Oxide Electrolyzer Cell for Hydrogen Production. *Int. J. Hydrog. Energy* **2009**, *34*, 7795–7806. [[CrossRef](#)]
47. Ni, M. Modeling of SOFC Running on Partially Pre-Reformed Gas Mixture. *Int. J. Hydrog. Energy* **2012**, *37*, 1731–1745. [[CrossRef](#)]